



# Crystallization Behavior and Morphology of Hexadecylamine-Modified Layered Zinc Phenylphosphonate and Poly(Butylene Succinate-co-Adipate) Composites with Controllable Biodegradation Rates

Dong-Lin Kuo<sup>1</sup> · Tzong-Ming Wu<sup>1</sup>

Published online: 15 October 2018

© Springer Science+Business Media, LLC, part of Springer Nature 2018

## Abstract

Hexadecylamine-modified zinc phenylphosphonate (m-PPZn) and biodegradable poly(butylene succinate-co-adipate) (PBSA) were melt mixed using a single-screw extruder. Experimental results of wide-angle X-ray diffraction (WAXD) and transmission electron microscopy revealed that the stacking layers of the m-PPZn were partially intercalated and partially exfoliated into the PBSA polymer matrix. The biodegradation rates of PBSA using lipase from *Pseudomonas* sp. increase as the contents of m-PPZn increase. The degree of crystallinity the lamellar thickness determined using WAXD and small-angle X-ray scattering data decrease as the loadings of m-PPZn increase. It is necessary to point out that the changes of degradation rate, the degree of crystallinity, and the lamellar thickness are almost linearly proportional to the loading of m-PPZn. This finding of composite materials with controllable degradation rate would provide an important information for the manufacturing PBSA nanocomposites used in biodegradable mulching films for agricultures.

**Keywords** Biocomposites · Degradation rate · Crystallization · Morphology

## Introduction

Biocompatible and biodegradable polymers have been attracted numerous attention owing to their promising biodegradability for environmental advantages [1]. Poly[(butylene succinate)-co-adipate] (PBSA), a semi-crystalline copolyester, shows plentifully desirable natures, including excellent chemical resistance, melt processability, and thermal properties, which is applicable in manufacturing mulching films and waste-composting bags [2–5]. As a consequence of more flexible polymer chains and slower crystallization rate of PBSA, useful application has been limited [6]. To enhance these physical properties, the loading of rigid inorganic material served as the nucleation agent into the biodegradable PBSA could improve its thermal and mechanical properties [7–11]. Ray et al. investigating the effect of adding various organically-modified

montmorillonite (o-MMT) on the morphology, mechanical properties, and viscoelastically of PBSA/o-MMT nanocomposites [7]. Chiu reported the incorporation of halloysite nanotube could enhance Young's and flexible moduli of PBSA [10].

Layered zinc phenylphosphonate (PPZn), a group of two-dimensional layered material, has received lots interest because of speed up the crystallization of various polymers [12–14]. However, the interlayer distance of PPZn is extremely small for the insertion of polymer chains into its interlayer gallery. To overcome this problem, organo-modifiers served as delamination compound to enlarge the interlayer spacing of PPZn have been applied [15, 16]. The biocompatible and nontoxic organo-modifiers were selected owing to the preparation of fully green nanocomposites. In the present study, the biocompatible and nontoxic hexadecylamine, a long-chain alkylamine, was used to manufacture the organically-modified PPZn (hereafter designated as m-PPZn) by co-precipitation technique. In our previous work, we only reported the degradation behavior of two different organically-modified PPZn polymer nanocomposites. The experimental results showed that the addition of organically-modified PPZn into the PBSA causes significant change of degradation rates for the nanocomposites as the

✉ Tzong-Ming Wu  
tmwu@dragon.nchu.edu.tw

<sup>1</sup> Department of Materials Science and Engineering,  
National Chung Hsing University, 250 Kuo Kuang Road,  
Taichung 402, Taiwan

contents of organically-modified PPZn increase [17]. The degradation rates of biodegradable nanocomposites were not linearly dependent on the contents of inorganic fillers, which is limited their applications in biodegradable mulching films for agricultures. Therefore the change of degradation rate of nanocomposites materials used as mulching films for agricultures need to be controllable with the loading of organically-modified PPZn due to various growing period of crops.

Thus, the new biodegradable PBSA/m-PPZn nanocomposites used for completely green materials with controllable degradation rate were prepared by a melt mixing process. The crystallization behavior, morphology and mechanical properties of PBSA/m-PPZn nanocomposites were studied systematically to understand the change of degradation rate.

## Experimental

### Materials

Biodegradable PBSA (Bionolle 3001) was obtained provided by Showa Denko Co., Ltd. According to the information provided from the supplier, it contained  $M_w = 190$  kg/mol,  $T_g = -43.8$  °C,  $T_m = 94.5$  °C. Hexadecylamine, polyoxyethylene bis(amine), phenylphosphonic acid, zinc nitrate, and lipase from *Pseudomonas* sp. were provided from Sigma-Aldrich.

Hexadecylamine-intercalated PPZns were prepared by a similar approach reported previously [15, 16]. Typically, the phenylphosphonic acid and zinc nitrate was individually dissolved in deionized water and mixed together followed by the addition of 0.1 M aqueous NaOH to reach pH 5–6. The prepared sample was filtered, washed, and dried at 60 °C under vacuum for 3 days. The 1, 3 and 5 wt.% PBSA/m-PPZn nanocomposites were fabricated by mixing the m-PPZn, PBSA, and polyoxyethylene bis(amine) as compatibilizer at 105 °C using a single-screw extruder (Brabender Mix 30/50E) for 5 min. For comparison, the pure PBSA was produced using the same method. Consequently, the fabricated PBSA and PBSA/m-PPZn samples were hot pressed at 105 °C to make a film for subsequent analyses.

### Methods

All specimens for biodegradation test were placed in 24-well plates containing 1 ml/mg enzymatic solution. The enzymatic solution were prepared using 0.1 M phosphate buffer, pH 7.4, at 37 °C with lipase from *Pseudomonas* sp. The specimens were taken out at 1, 2, 3, and 4 days, washed with distilled water and vacuum dried. The degree of degradation was calculated using the equation:  $W_{weight\ loss}(\%) = 100[(W_0 - W_t)/W_0]$ , where  $W_0$  corresponds to the original weight of a specimen and  $W_t$  represents the weight of a

specimen after different degradation times. The experimental data revealed here are the mean values of at least three measurements.

For the degradation tests, the molecular weights of all samples were evaluated using gel permeation chromatography (GPC, Waters 717 Plus autosampler). Calibration was performed using polystyrene standards.

X-ray diffractometer (Bruker D8) equipped with a Ni-filtered Cu K $\alpha$  radiation ( $\lambda = 1.54$  Å) was used for the experiments of small-angle X-ray scattering (SAXS) and wide-angle X-ray diffraction (WAXD). The diffraction patterns of WAXD measurements were performed in the range of  $2\theta = 1.5^\circ - 30^\circ$  at a scanning rate of  $1^\circ/\text{min}$ . The degree of crystallinity was calculated by WAXD data. The  $q$ , defined as  $q = (4\pi\sin\theta)/\lambda$ , is the scattering vector in SAXS measurement.

The transmission electron microscopy (TEM) was carried out by a Hitachi HF-2000. The specimens of TEM experiments encapsulated in epoxy matrix were obtained by a Reichert Ultracut ultramicrotome. Field-emission scanning electron microscopy (FESEM, JEOL JSM-6700F) was used to examine the surface morphologies of all samples. The surfaces of all samples were covered with gold to prevent charging.

The isothermal crystallization behavior was carried out by a PerkinElmer Pyris Diamond differential scanning calorimeter (DSC) and all experiments were performed under a nitrogen atmosphere. All specimens were heated to 150 °C at a rate of  $10^\circ\text{C}/\text{min}$  and held for 5 min to remove the residual crystals. Then, they were quickly quenched to proposed crystallization temperatures ( $T_{cs}$ ) between 62 and 70 °C, and held to finish total crystallization.

The growth of spherulite was obtained using a Zeiss optical microscope equipped with a Mettler FP-82 hot stage and crossed polarizers. All samples were heated to melt at 150 °C at a rate of  $10^\circ\text{C}/\text{min}$  for 3 min to remove previous thermal history. Consequently, the samples were then cooled rapidly to the  $T_{cs}$ . Optical microscopy was recorded at the proposed  $T_c$  for various times.

The storage modulus ( $E'$ ) of the PBSA/m-PPZn nanocomposites was performed on a Perkin Elmer dynamic mechanical analyzer (DMA) in a temperature range of  $-60$  to  $20$  °C at  $2$  °C/min heating rate and 1 Hz constant frequency.

## Results and Discussion

### Characterization and Mechanical Properties of PBSA/m-PPZn Nanocomposites

Figure 1 reveals the WAXD scans of PPZn, m-PPZn and 5 wt.% PBSA/m-PPZn nanocomposites. The WAXD data

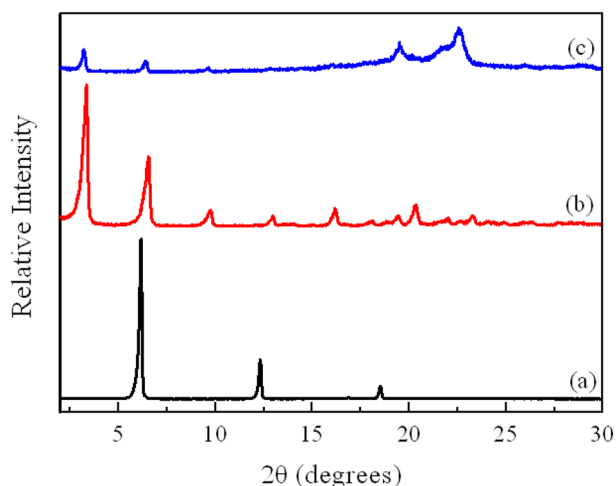


**Fig. 1** X-ray diffraction patterns of **a** PPZn, **b** m-PPZn and **c** 5 wt.% PBSA/m-PPZn nanocomposite

show that several strong diffraction peaks of PPZn and m-PPZn were obtained. The main diffraction peak of PPZn observed at  $2\theta = 6.31^\circ$  agreed well with the previous literatures [15, 16]. The diffraction peaks of m-PPZn were obtained at  $2\theta = 3.21^\circ$  and  $6.40^\circ$ . These results demonstrate that the interlayer spacing determined using Bragg's equation ( $2d \sin\theta = \lambda$ ) was at 27.5 Å and 13.8 Å, respectively [18, 19]. The interlayer spacing of PPZn is extensively expanded with the addition of hexadecylamine through the interaction of ionic exchange. As the curve (c) presented in this figure, the diffraction peaks of PBSA/m-PPZn nanocomposites at  $2\theta = 19.4^\circ$ ,  $21.5^\circ$ , and  $22.5^\circ$  suggested the crystal structure of PBSA/m-PPZn nanocomposites is the same compared to that of PBS [9, 20]. The diffraction peak of m-PPZn at  $2\theta = 3.21^\circ$  was observed and slightly shifted to the lower angle for the PBSA/m-PPZn nanocomposites. This implies that the PBSA polymer chain is intercalated into the m-PPZn galleries. This phenomenon probably results from disordered intercalated nanocomposite [21]. Therefore, the morphology of PBSA/m-PPZn nanocomposites was examined by TEM analysis. Figure 2 reveals TEM micrographs of 5 wt.% PBSA/m-PPZn nanocomposites. This data shows that the intercalated and agglomerated structures were observed.

Figure 3 displays the temperature dependence of storage modulus  $E'$  of neat PBSA and the corresponding nanocomposites over a temperature range of  $-60$  to  $20^\circ\text{C}$ . It can be seen that the  $E'$  of PBSA at  $-60^\circ\text{C}$  is about 3340 MPa and decreases with the increasing temperature. This result suggests that the molecular motion of PBSA is insufficient in the glassy region, whereas above the glass transition temperature, the thermal energy becomes comparable to the potential energy barriers to the molecular motions. The  $E'$  of the PBSA/m-PPZn nanocomposites at  $-60^\circ\text{C}$  are approximately estimated to be 3410, 3570, and 3980 MPa for 1, 3,

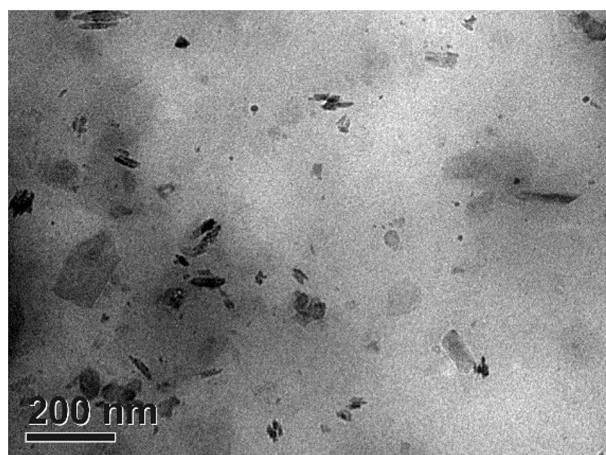


**Fig. 2** TEM micrographs of 5 wt.% PBSA/m-PPZn nanocomposites

and 5 wt.% loading of m-PPZn. These results show that the  $E'$  of the PBSA/m-PPZn nanocomposites increased with increasing m-PPZn content. This increase may be attributed to the reinforcement effect of the presence of the rigid m-PPZn layers, leading to the prominent improvement on the stiffness of the PBSA matrix.

### Biodegradation and Morphology of PBSA/m-PPZn Nanocomposites

The microbial biodegradability of PBSA/m-PPZn nanocomposites was shown in Fig. 4. It can be seen that the degradation rates of all nanocomposites showed similar tendency compared to that of neat PBSA matrix and the weight loss of PBSA/m-PPZn nanocomposites increases as the degradation time increases. The degradation rate of the neat PBSA is slowest, but the degradation rate of the 5 wt.%

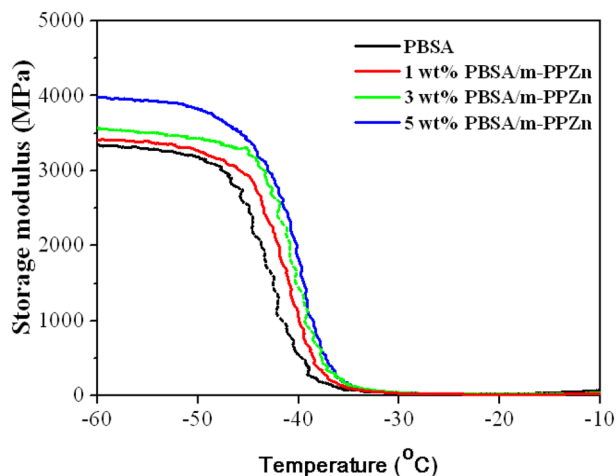


**Fig. 3** Dependence of the storage modulus on temperature of PBSA/m-PPZn nanocomposites

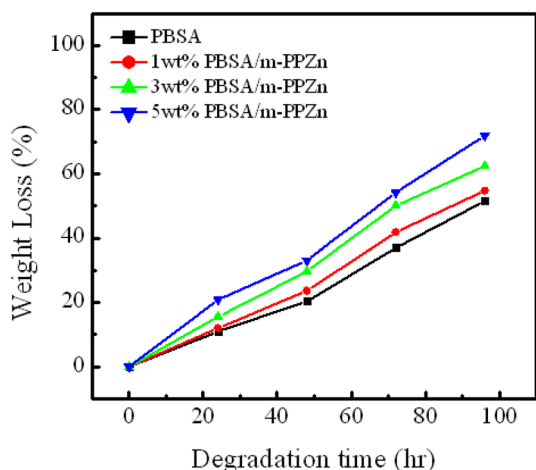


**Fig. 4** Dependence of the weight loss on the degradation time of PBSA/m-PPZn nanocomposites

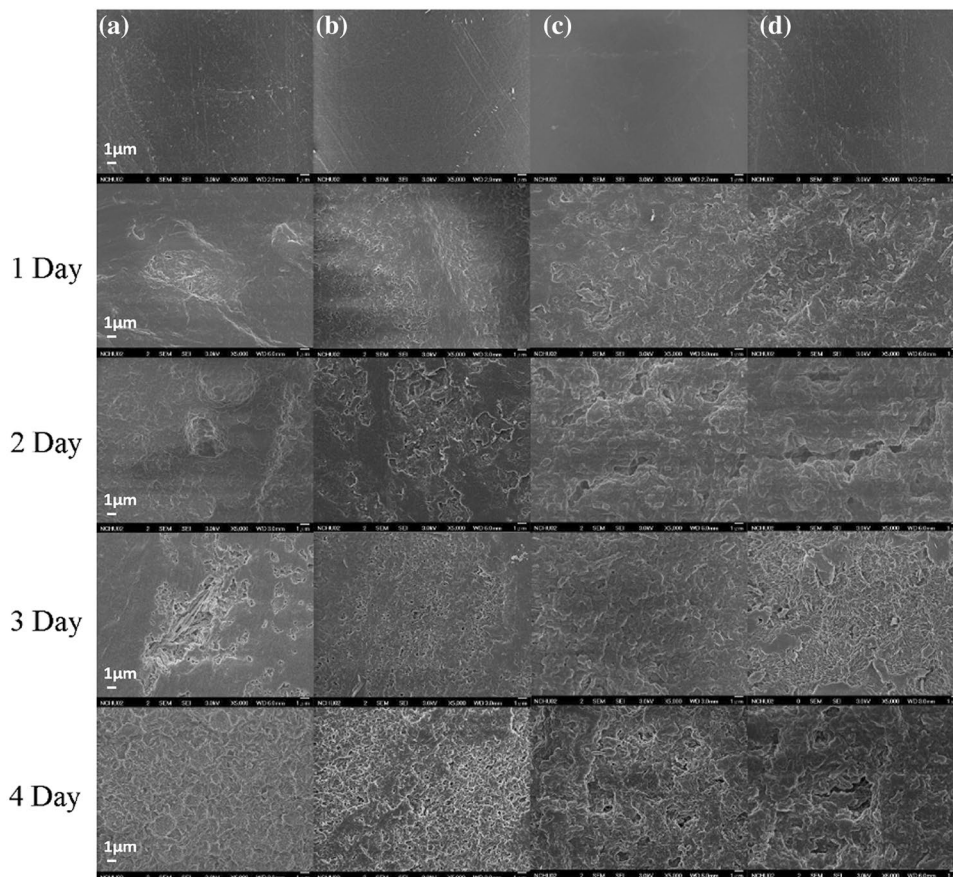
PBSA/m-PPZn nanocomposites is fastest compared to those of PBSA/m-PPZn nanocomposites. While the weight loss of the PBSA reached 51.5% after 96-h incubation, the weight loss of the 1 wt.% PBSA/m-PPZn, 3 wt.% PBSA/m-PPZn and 5 wt.% PBSA/m-PPZn nanocomposites were 54.8, 62.4, and 71.9%, respectively. It is necessary to point out that the

changes of degradation rate are almost linearly proportional to the loading of m-PPZn. The possible explanation of this behavior would be studied using SAXS, WAXD, DSC and polarized optical microscopy (POM).

To observe the change of morphologies for all the specimens subsequent to the degradation, the analysis technique of FESEM can be applied. The FESEM images of the surfaces before and after microbial degradation are presented in Fig. 5. Before degradation, all samples show similar morphology and the surfaces of PBSA were pretty flat compared to those of the nanocomposites. The surface condition of PBSA/m-PPZn nanocomposites got more and more damaged within the incubation time course. After 2 days of incubation, the surface wearing away with the presence of small amount of porous structures on PBSA were obtained. After the same degradation time, the surface erosion of all nanocomposites contains more porous and holes structures. It can also be observed that the roughness of the PBSA nanocomposites surface as the loading of m-PPZn increases, demonstrating that the addition of the m-PPZn into PBSA polymer matrix improves the degradation rate of PBSA.

In order to study the effect of m-PPZn on the structures of PBSA matrix, the SAXS analysis was performed. The Lorentz-corrected SAXS data of PBSA/m-PPZn nanocomposites isothermal crystallization at 66 °C are shown

**Fig. 5** FESEM images of the microbially degraded **a** neat PBSA, **b** 1 wt.% PBSA/m-PPZn, **c** 3 wt.% PBSA/m-PPZn, and **d** 5 wt.% PBSA/m-PPZn nanocomposites. All figures have the same magnifications



in Fig. 6. To calculate the morphological factors, such as the amorphous thickness ( $l_a$ ), the lamellar thickness ( $l_c$ ), and long period ( $L_p = l_a + l_c$ ), of all the materials, we used a one-dimensional correlation function. The one-dimensional correlation function, which is the Fourier transformation of Lorentz-corrected SAXS profiles, was evaluated as the following equation [22, 23]:

$$\gamma(z) = \frac{1}{Q} \int_0^{\infty} qI^2(q) \cos(qz) dq \quad (1)$$

where  $z$  is the correlation distance,  $Q$  is a scattering invariant, and  $I(q)$  is the experimental SAXS intensity corrected for thermal fluctuations.

The curves of one-dimensional correlation function of PBSA/m-PPZn nanocomposites are revealed in Fig. 7. The morphological factors of the nanocomposites calculated from the one-dimensional correlation function are presented in Table 1. For the PBSA/m-PPZn nanocomposites,  $L_p$  and  $l_c$  values progressively decrease with the increasing m-PPZn contents. The change of  $l_c$  is almost linearly proportional to the loading of m-PPZn. This result is probably contributed to the presence of hexadecylamine served as intercalation agents for PPZn, which might prevent the crystalline packing of PBSA crystallites. In addition, the  $l_a$  values slightly increase with the addition of m-PPZn. Therefore, the degree of crystallinity of the nanocomposites determined using WAXD data was almost linearly decreased as the loading of m-PPZn.

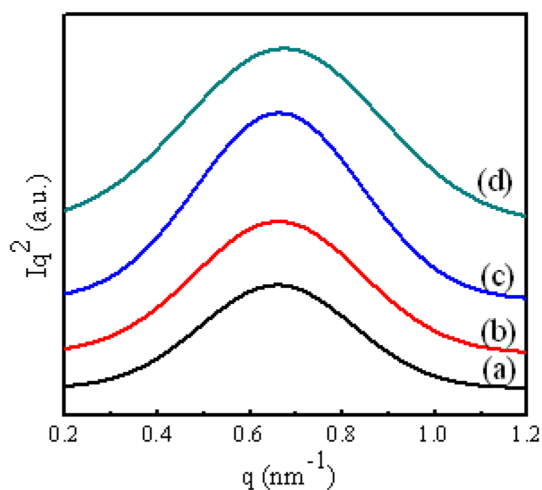


**Fig. 6** Lorentz-corrected SAXS intensity profiles of **a** neat PBSA, **b** 1 wt.% PBSA/m-PPZn, **c** 3 wt.% PBSA/m-PPZn, and **d** 5 wt.% PBSA/m-PPZn nanocomposites during isothermal crystallization at 66 °C

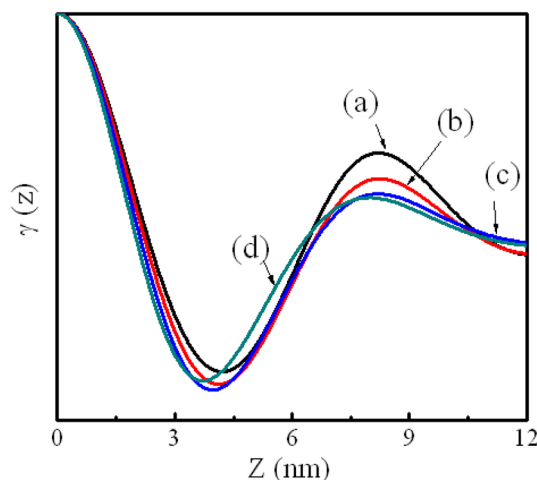


**Fig. 7** One-dimensional correlation function calculated from the SAXS profiles of **a** neat PBSA, **b** 1 wt.% PBSA/m-PPZn, **c** 3 wt.% PBSA/m-PPZn, and **d** 5 wt.% PBSA/m-PPZn nanocomposites during isothermal crystallization at 66 °C

### Crystallization Behavior of PBSA/m-PPZn Nanocomposites

The isothermal crystallization kinetics of PBSA and PBSA/m-PPZn nanocomposites are determined by the following Avrami equation [24, 25]:

$$1 - X_t = \exp(-kt^n) \quad (2)$$

where  $k$  and  $n$  are the Avrami parameters, depending on the nucleation and growth mechanisms of crystallites. The  $X_t$  is relative crystallinity at crystallization time  $t$ . In order to adapt easily with the operation, Eq. (2) can be rewritten into the following equation as Eq. (3).

$$\ln[-\ln(1 - X_t)] = n \ln t + \ln k \quad (3)$$

The crystallization half-time ( $t_{1/2}$ ) is defined as the time taken from the onset of the relative crystallinity until 50% completion, which is illustrated as Eq. (4).

$$t_{1/2} = \left( \frac{\ln 2}{k} \right)^{1/n} \quad (4)$$

**Table 1** Structural parameters of PBSA and PBSA/m-PPZn nanocomposites crystallized at  $T_c$  of 66 °C estimated by XRD and SAXS measurements

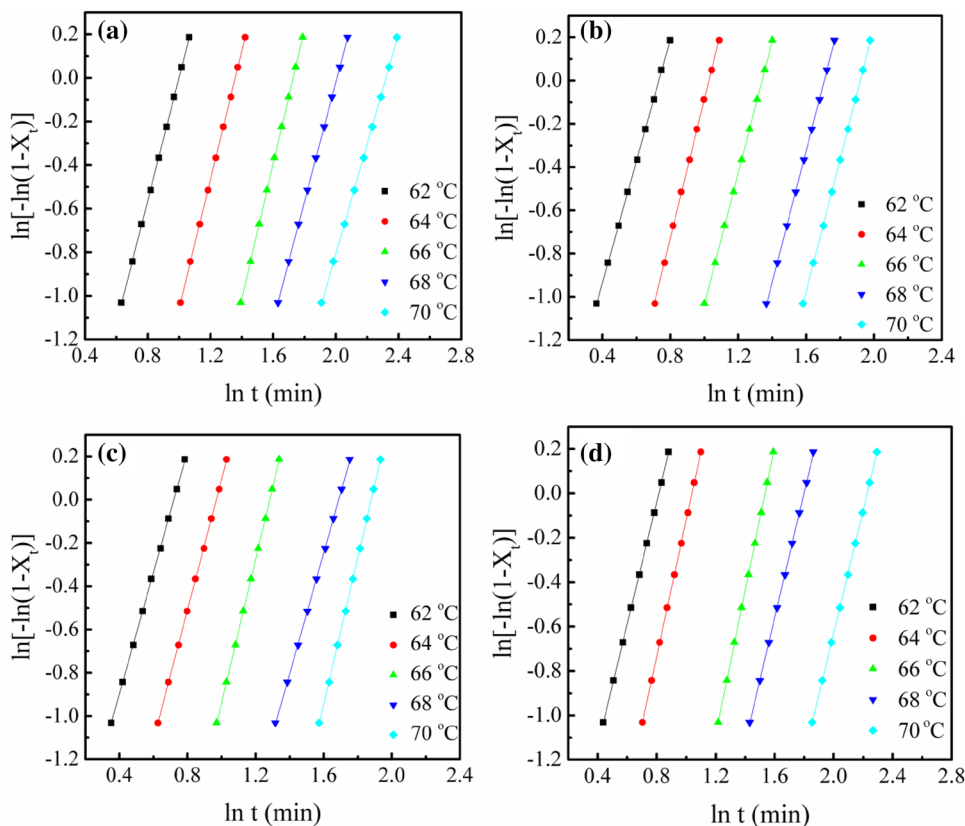
Sample	Temp. (°C)	$X_c$ (%)	$L_p$ (nm)	$l_c$ (nm)	$l_a$ (nm)
PBSA	66	47.09	8.24	3.40	4.84
1 wt.% PBSA/m-PPZn	66	46.42	8.23	3.33	4.90
3 wt.% PBSA/m-PPZn	66	42.83	8.19	3.23	4.96
5 wt.% PBSA/m-PPZn	66	40.14	7.99	3.11	4.88

The plots of  $\ln[-\ln(1 - X_t)]$  versus  $\ln t$  for PBSA/m-PPZn nanocomposites are showed in Fig. 8. All drawings show similar tendency, suggesting that the crystallization mechanism of PBSA/m-PPZn nanocomposites at various  $T_{cs}$  remains the same. The  $n$  values,  $k$  values, and  $t_{1/2}$  at various  $T_{cs}$  are summarized in Table 2. The  $n$  value used in the Avrami expression represents the mechanism of crystal growth and nucleation. The  $n$  values of PBSA listed in Table 2 are found to range from 2.52 to 3.09. Generally, the  $n$  values near to 3 are assigned to an athermal nucleation process subsequently a three-dimensional crystal growth. The  $n$  values of PBSA/m-PPZn nanocomposites ranged from 2.75 to 3.38 are similar to those of PBSA. Thus, these data propose that the incorporation of m-PPZn into the PBSA does not alter the mechanism of PBSA crystallization. Additionally,  $t_{1/2}$  for the all samples shown in Table 2 increases as  $T_c$  increases, recommending that the isothermal crystallization rate decreases with increasing  $T_c$ , owing to the lower supercooling at higher  $T_c$ . With the additional loading of 3 wt.% m-PPZn into PBSA, the  $t_{1/2}$  significantly decreases as the content of m-PPZn increases. For example, the  $t_{1/2}$  values of PBSA decrease remarkably from 8.80 to 5.88 min in nanocomposites with 3 wt.% m-PPZn contents when crystallized at  $T_c = 70^\circ\text{C}$ . This implies that m-PPZn could speed up the crystallization of PBSA in the nanocomposites. Nevertheless, by

**Table 2** Kinetic parameters of neat PBSA and PBSA/m-PPZn nanocomposites isothermally melt crystallized at  $T_c = 62\text{--}70^\circ\text{C}$

Sample	$T_c$ ( $^\circ\text{C}$ )	$n$	$k$ ( $\text{min}^{-n}$ )	$t_{1/2}$ (min)	$G$ ( $\mu\text{m/s}$ )
PBSA	62	2.82	$5.9 \times 10^{-2}$	2.39	1.429
	64	2.95	$1.82 \times 10^{-2}$	3.43	1.304
	66	3.09	$4.81 \times 10^{-3}$	5.00	1.083
	68	2.74	$4.10 \times 10^{-3}$	6.51	0.901
	70	2.52	$2.88 \times 10^{-3}$	8.80	0.700
1wt.% PBSA/m-PPZn	62	2.81	$1.28 \times 10^{-1}$	1.83	1.160
	64	3.20	$3.74 \times 10^{-2}$	2.49	0.988
	66	3.04	$1.69 \times 10^{-2}$	3.39	0.821
	68	3.03	$5.58 \times 10^{-3}$	4.89	0.618
	70	3.06	$2.82 \times 10^{-3}$	6.05	0.444
3wt.% PBSA/m-PPZn	62	2.81	$1.33 \times 10^{-1}$	1.80	1.055
	64	3.01	$5.43 \times 10^{-2}$	2.33	0.851
	66	3.32	$1.42 \times 10^{-2}$	3.23	0.665
	68	2.79	$8.97 \times 10^{-3}$	4.74	0.520
	70	3.38	$1.73 \times 10^{-3}$	5.88	0.347
5wt.% PBSA/m-PPZn	62	2.75	$1.07 \times 10^{-1}$	1.98	0.930
	64	3.07	$4.11 \times 10^{-2}$	2.51	0.768
	66	3.25	$6.83 \times 10^{-3}$	4.15	0.583
	68	2.81	$6.35 \times 10^{-3}$	5.30	0.442
	70	2.77	$2.10 \times 10^{-3}$	8.13	0.268

**Fig. 8** Avrami plots of **a** neat PBSA, **b** 1 wt.% PBSA/m-PPZn, **c** 3 wt.% PBSA/m-PPZn, and **d** 5 wt.% PBSA/m-PPZn nanocomposites isothermal crystallization at various temperatures



adding m-PPZn into PBSA up to 5 wt.%, the  $t_{1/2}$  of the PBSA/m-PPZn nanocomposite was remarkably increased. These data indicate that high loading of m-PPZn might reduce the free volume of the polymer and then delay the diffusion and migration of PBSA polymer chains to the crystalline packing and formation owing to the restriction effects, causing the increase of  $t_{1/2}$ .

The nucleation and crystalline morphologies of PBSA/m-PPZn nanocomposites were studied using polarized optical micrographs to supplementary expose the crystallization behaviors of the PBSA/m-PPZn nanocomposites. Figure 9 illustrates the growth of spherulites isothermally crystallized at 66 °C. The number of spherulites of the PBSA/m-PPZn nanocomposites at the same  $T_c$  clearly increases and the spherulite size decreases by adding 3 wt.% m-PPZn. This result indicates that the incorporation of m-PPZn increased the amount of heterogeneous nucleation in the PBSA matrix. Nevertheless, the spherulite size of 5 wt.% PBSA/m-PPZn nanocomposite turns out to be bigger, and the number of nucleation point and spherulites becomes less as the addition of 5 wt.% m-PPZn. This finding reveals that high loading of m-PPZn could prevent the PBSA chain motion due to the possible interaction of m-PPZn and organic modifier, causing the reduction of nucleation.

The effects of m-PPZn on the PBSA spherulitic growth rate ( $G$ ) shown in Table 2 were also determined using POM data. It is found that the  $G$  values decreased as  $T_c$  increases and the  $G$  values at a specified  $T_c$  decreased with the increase in the weight fraction of m-PPZn.

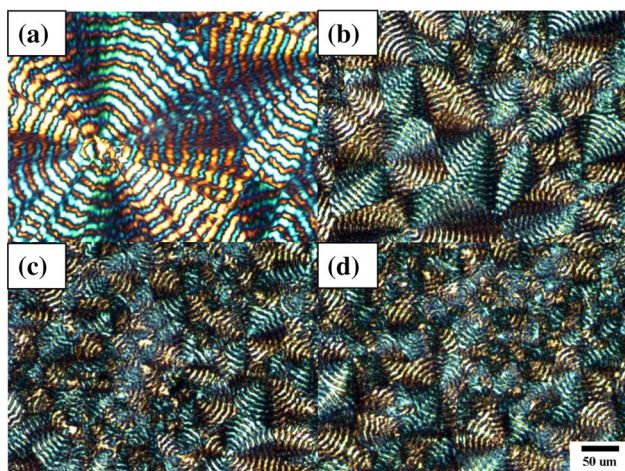


**Fig. 9** Optical micrographs of spherulites of **a** neat PBSA, **b** 1 wt.% PBSA/m-PPZn, **c** 3 wt.% PBSA/m-PPZn, and **d** 5 wt.% PBSA/m-PPZn nanocomposites during isothermal crystallization at 66 °C

## Degradation Mechanism of PBSA/m-PPZn Nanocomposites

It is recognized that internal structural factors and external environmental factors, such as chemical structure, degree of crystallinity, microstructure, molecular weight, temperature, relative humidity, and pH value, have an effect on the degradation rate of biodegradable polymers [26]. This study of the microbial degradation was designed with the same external environment condition. Besides, the chemical structure for PBSA matrix is the same and initial molecular weight for PBSA matrix is almost identical. The only difference in this study is mainly contributed from the degree of crystallinity and the microstructure, such as the lamellar thickness. In accordance with the WAXD data, the ranking of degree of crystallinity and lamellar thickness was PBSA > 1 wt.% PBSA/m-PPZn nanocomposites > 3 wt.% PBSA/m-PPZn nanocomposites > 5 wt.% PBSA/m-PPZn nanocomposites. For 5 wt.% PBSA/m-PPZn nanocomposites, the fastest degradation rate was achieved due to the lowest degree of crystallinity and lamellar thickness. Thus, the degradation rate altered in the ranking 5 wt.% PBSA/m-PPZn nanocomposites > 3 wt.% PBSA/m-PPZn nanocomposites > 1 wt.% PBSA/m-PPZn nanocomposites > neat PBSA. It is also necessary to point out that the change of degree of crystallinity, lamellar thickness, and degradation rate are almost linearly proportional to the loading of hexadecylamine-modified PPZn, which is totally different from other organically-modified PPZn/PBSA systems [17]. In order to control the degradation rate, the change of crystallinity and lamellar thickness of nanocomposites needs to be controlled. This finding would provide a important information for the manufacturing PBSA nanocomposites used in biodegradable mulching films for agricultures.

Two categories, such as the exo- and endo-type hydrolysis activity, were used to explain the degradation behavior of biodegradable polymers. They considerably depend on the change of weight-average molecular weight ( $M_w$ ) of the biodegradable polymers [27]. The exo-type hydrolysis activity is followed if the  $M_w$  does not vary extensively during the degradation process. This degradation behavior reveals that the degradation initiates from both sides of the PBSA polymer chains. In contrast, the endo-type hydrolysis activity is obeyed if  $M_w$  significantly decreases during the degradation process. This occurrence is ascribed to the degradation begins at the midpoint of the PBSA polymer chain. The  $M_w$  change of PBSA/m-PPZn nanocomposites after microbial degradation is shown in Fig. 10. The polymer dispersity index (PDI) of all samples is recorded in Table 3. This result indicates that the change of  $M_w$  of PBSA is very little as the weight loss of PBSA steadily increases. Therefore, the degradation behavior of the PBSA is contributed to the exo-type hydrolysis activity, which is in good agreement

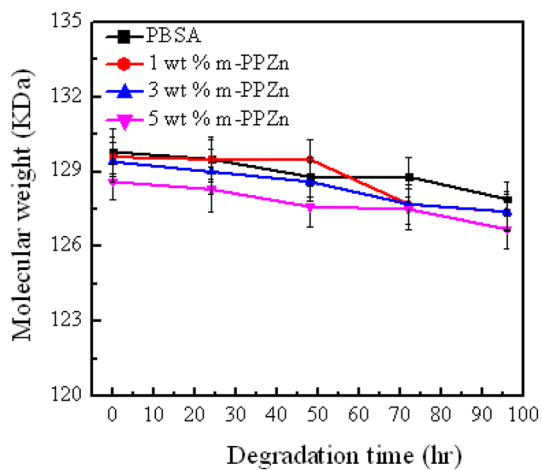


**Fig. 10** Molecular weight of residual PBSA/m-PPZn nanocomposites after the microbial degradation

**Table 3** PDI of PBSA/m-PPZn obtained by GPC measurements with various degradation times

Sample	PDI				
	0 h	24 h	48 h	72 h	96 h
PBSA	1.47	1.50	1.51	1.53	1.59
1 wt.% PBSA/m-PPZn	1.47	1.48	1.53	1.52	1.57
3 wt.% PBSA/m-PPZn	1.48	1.50	1.54	1.54	1.61
5 wt.% PBSA/m-PPZn	1.49	1.54	1.55	1.59	1.64

with the previous studies [27, 28]. Nevertheless, the degradation performance of PBSA/m-PPZn nanocomposites is extremely analogous to those of PBSA. These data point out that the addition of the m-PPZn into PBSA does not alter the degradation performance of PBSA.

## Conclusions

The new biocompatible and biodegradable PBSA/m-PPZn nanocomposites with controllable degradation rates were manufactured using a melt mixing process. The results of WAXD and TEM revealed that the structure of PBSA/m-PPZn nanocomposites contained the mixture of exfoliated and intercalated form. Degradation tests results show that the weight loss of PBSA almost linearly increases as the loading of m-PPZn increases. This result is attributed to the lower degree of crystallinity and lamellar thickness for the PBSA/m-PPZn nanocomposites. This finding would provide an important information for the manufacturing PBSA nanocomposites used in biodegradable mulching films for agricultures.

**Acknowledgements** The work was supported by the Ministry of Science and Technology (MOST) under Grant MOST 104-2212-E-005-089-MY2 and the Ministry of Education under the project of Innovation and Development Center of Sustainable Agriculture (IDCSA).

## References

- Ojijo V, Ray SS (2014) Nano-biocomposites based on synthetic aliphatic polyesters and nanoclay. *Prog Mater Sci* 62:1
- Chen YA, Hang YT, Wu TM (2015) Polymorphism and spherulite morphology of poly(1,4-butylene adipate)/organically-modified layered double hydroxide nanocomposites. *J Appl Polym Sci* 132:42526
- Ray SS, Bousmina M, Okamoto K (2005) Structure and properties of nanocomposites based on poly (butylene succinate-*co*-adipate) and organically modified montmorillonite. *Macro Mater Eng* 290:759
- Qi Z, Ye H, Xu J, Chen J, Guo B (2013) Improved the thermal and mechanical properties of poly(butylene succinate-*co*-butylene adipate) by forming nanocomposites with attapulgite. *Colloids Surf A Physicochem Eng Asp* 421:109
- Lichocik M, Owczarek M, Miros P, Guzińska K, Gutowska A, Ciechańska D, Krucińska I, Siwek P (2012) Impact of PBSA (Bionolle) biodegradation products on the soil microbiological structure. *Fibers Text East Eur* 20:179
- Bandyopadhyay J, Al-Thabaiti SA, Ray SS, Basahel SN, Mokhtar M (2014) Unique cold-crystallization behavior and kinetics of biodegradable poly[(butylene succinate)-*co* adipate] nanocomposites: a high speed differential scanning calorimetry study. *Macromol Mater Eng* 299:939
- Ojijo V, Malwela T, Ray SS, Sadiku R (2012) Unique isothermal crystallization phenomenon in the ternary blends of biopolymers polylactide and poly[(butylene succinate)-*co*-adipate] and nanoclay. *Polymer* 53:505
- Ojijo V, Ray SS, Sadiku R (2012) Effect of nanoclay loading on the thermal and mechanical properties of biodegradable polylactide/poly[(butylene succinate)-*co*-adipate] blend composites. *ACS Appl Mater Interfaces* 4:2395
- Chen YA, Tsai GS, Chen EC, Wu TM (2016) Crystallization behaviors and microstructures of poly(butylene succinate-*co*-adipate)/modified layered double hydroxide nanocomposites. *J Mater Sci* 51:4021
- Chiu FC (2016) Fabrication and characterization of biodegradable poly(butylene succinate-*co*-adipate) nanocomposites with halloysite nanotube and organomontmorillonite as nanofiller. *Polym Test* 54:1
- Chiu FC (2017) Halloysite nanotube- and organoclay-filled biodegradable poly(butylene succinate-*co*-adipate)/maleated polyethylene blend-based nanocomposites with enhanced rigidity. *Compos Part B Eng* 110:193
- Pan P, Liang Z, Cao A, Inoue Y (2009) Layered metal phosphonate reinforced poly(L-lactide) composites with a highly enhanced crystallization rate. *ACS Appl Mater Interfaces* 1:402
- Xu T, Wang Y, He D, Xu Y, Li Q, Shen C (2014) Nucleation effect of layered metal phosphonate on crystallization of isotactic polypropylene. *Polym Test* 34:131
- Wu N, Wang H (2013) Effect of zinc phenylphosphonate on the crystallization behavior of poly (L-lactide). *J Appl Polym Sci* 130:2744
- Chen YA, Chen EC, Wu TM (2016) Lamellae evolution of stereocomplex-type poly(lactic acid)/organically-modified layered zinc phenylphosphonate nanocomposites induced by isothermal crystallization. *Materials* 9:159



16. Chen YA, Chen EC, Wu TM (2015) Organically modified layered zinc phenylphosphonate reinforced stereocomplex-type poly (lactic acid) nanocomposites with highly enhanced mechanical properties and degradability. *J Mater Sci* 50:7770
17. Chen YA, Kuo DL, Chen EC, Wu TM (2017) Enhanced enzymatic degradation in nanocomposites of various organically-modified layered zinc phenylphosphonate and poly(butylene succinate-*co*-adipate). *J Polym Res* 24:212
18. Poojary DM, Clearfield A (1995) Coordinative intercalation of alkylamines into layered zinc phenylphosphonate. Crystal structures from X-ray powder diffraction data. *J Am Chem Soc* 117:11278
19. Zhang Y, Scott KJ, Clearfield A (1995) Intercalation of alkylamines into dehydrated and hydrated phenylphosphonates. *J Mater Chem* 5:315
20. Chen YA, Tsai GS, Chen EC, Wu TM (2017) Thermal degradation behaviors and biodegradability of novel nanocomposites based on various poly[(butylene succinate)-*co*-adipate] and modified layered double hydroxides. *J Taiwan Inst Chem Eng* 77:263
21. Gilman JW, Morgan AB (2003) Characterization of polymer-layered silicate (clay) nanocomposites by transmission electron microscopy and X-ray diffraction: a comparative study. *J Appl Polym Sci* 87:1329
22. Strobl G, Schneider M (1980) Direct evaluation of the electron density correlation function of partially crystalline polymers. *J Polym Sci Polym Phys Ed* 18:1343
23. Barbi V, Funari SS, Gehrke R, Scharnagl N, Stribeck N (2003) SAXS and the gas transport in polyether-block-polyamide copolymer membranes. *Macromolecules* 36:749
24. Avrami M (1941) Granulation, phase change, and microstructure kinetics of phase change. III. *J Chem Phys* 9:177
25. Avrami M (1940) Kinetics of phase change. II Transformation-time relations for random distribution of nuclei. *J Chem Phys* 8:212
26. Numata K, Finne-Wistrand A, Albertsson AC, Doi Y, Abe H (2008) Enzymatic degradation of monolayer for poly(lactide) revealed by real-time atomic force microscopy: effects of stereochemical structure, molecular weight, and molecular branches on hydrolysis rates. *Biomacromolecules* 9:2180
27. Ando Y, Yoshikawa K, Yoshikawa T, Nishioka M, Ishioka R, Yakabe Y (1998) Biodegradability of poly(tetramethylene succinate-*co*-tetramethylene adipate): I. Enzymatic hydrolysis. *Polym Degrad Stab* 61:129
28. Ciou CY, Li SY, Wu TM (2014) Morphology and degradation behavior of poly (3-hydroxybutyrate-*co*-3-hydroxyvalerate)/layered double hydroxides composites. *Eur Polym J* 59:136